Rock dissolution patterns and geochemical shutdown of CO_2-brine-carbonate reactions during convective mixing in porous media

X. Fu[1], L. Cueto-Felgueroso[1,2], D. Bolster[3] and R. Juanes[1,†]

[1]Department of Civil & Environmental Engineering, Massachusetts Institute of Technology, Cambridge, MA 02139, USA

[2]Civil Engineering School, Technical University of Madrid, Madrid, Spain

[3]Department of Civil & Environmental Engineering & Earth Sciences, University of Notre Dame, Notre Dame, IN 46556, USA

Motivated by the process of CO_2 convective mixing in porous media, here we study the formation of rock-dissolution patterns that arise from geochemical reactions during Rayleigh–Bénard–Darcy convection. Under the assumption of instantaneous chemical equilibrium, we adopt a formulation of the local reaction rate as a function of scalar dissipation rate—a measure that depends solely on flow and transport—and chemical speciation, which is a measure that depends only on the equilibrium thermodynamics of the chemical system. We use high-resolution simulations to examine the interplay between the density-driven hydrodynamic instability and the rock dissolution reactions, and analyze the impact of geochemical reactions on the macroscopic mass exchange rate. We find that dissolution of carbonate rock initiates in regions of locally high mixing, but that the geochemical reaction shuts down significantly earlier than shutdown of convective

† Email address for correspondence: juanes@mit.edu

mixing. This early shutdown feature reflects the important role that chemical speciation

plays in this hydrodynamics–reaction coupled process. Finally, we extend our analysis to

three dimensions and explore the morphology of dissolution patterns in 3D.

Key words: CO_2 sequestration; convective mixing; geochemical reactions; pattern formation; reactive transport

---

1. Introduction

Convective mixing in porous media is an important process that has been studied extensively (Nield & Bejan 2006). Recently, it has received renewed attention in the context of geologic sequestration of carbon dioxide (CO_2), a promising technology to mitigate climate change by reducing atmospheric greenhouse gas emissions (Lackner 2003; Orr 2009; Szulczewski *et al.* 2012). The sequestration process involves the capture of CO_2 from anthropogenic sources such as coal-fired and gas-fired power plants, the transportation after compression through a pipeline system and, finally, the injection of supercritical CO_2 into underground geologic formations such as deep saline aquifers (IPCC 2005). Once it reaches a brine-saturated porous formation, CO_2 dissolves into the ambient brine, creating a solution that is denser than both initial fluids. The density increase triggers a Rayleigh–Bénard-type gravitational instability that enables mass transport through advection and diffusion—known here as convective mixing—rather than diffusion alone (Weir *et al.* 1996; Lindeberg & Wessel-Berg 1997; Ennis-King & Paterson 2005; Riaz *et al.* 2006). Convective mixing allows for faster solubility trapping of CO_2 into the brine, thus increasing storage security against leakage risks (MacMinn *et al.* 2011; Szulczewski *et al.* 2012).

Solubility trapping of CO_2 into groundwater at reservoir conditions (e.g. $pCO_2 \sim$ 10 MPa, T $\sim$ 60°C) creates an acidic solution with pH $\sim$ 4 (Xu *et al.* 2010). As suggested by recent core flood experiments on carbonate rock samples (Carroll *et al.* 2013; Elkhoury *et al.* 2013), interaction between the acidic CO_2-brine solution and carbonate rocks leads to dissolution of minerals such as calcite ($CaCO_3$) through a series of geochemical reactions. Under constant flow conditions, rock dissolution may lead to the formation of high-porosity channels in the core sample (Carroll *et al.* 2013). To put this in the context of CO_2 sequestration, as mineral dissolution occurs in response to the lowered pH in brine, this could result in a positive feedback that further drives the solubility trapping of CO_2 and mineral dissolutions (Xu *et al.* 2003). A recent study addressed this issue by performing a series of two-dimensional aquifer simulations that incorporate geochemistry into existing flow simulation software (Saaltink *et al.* 2013). They concluded that porosity changes due to calcite dissolution were relatively small in the scenario they studied.

Here, we revisit this problem using high-resolution simulation. The phenomenon of convective mixing has been studied through nonlinear simulations in two dimensions (e.g., Riaz *et al.* 2006; Hassanzadeh *et al.* 2007; Hidalgo & Carrera 2009; Neufeld *et al.* 2010; Hidalgo *et al.* 2012; Szulczewski *et al.* 2013; Bolster 2014; Slim 2014), three dimensions (Pau *et al.* 2010; Fu *et al.* 2013), and experimental systems reproducing the conditions for a stationary horizontal layer (Neufeld *et al.* 2010; Kneafsey & Pruess 2010; Backhaus *et al.* 2011; Slim *et al.* 2013) or a migrating buoyant current (MacMinn *et al.* 2012; MacMinn & Juanes 2013). In the case of three-dimensional simulations, a striking self-organized network pattern is observed near the top boundary layer (Fu *et al.* 2013). Here, we study the morphology of rock dissolution patterns that develop from the interplay between reaction and density-dependent flow and ask the following questions: how do flow patterns

translate into spatial organization of the permeability field through mineral dissolution?

What is the evolution that leads to this pattern morphology? As rock dissolution alters

local porosity and permeability, how does their change, in turn, affect flow and transport?

We seek answers to these questions through high-resolution three-dimensional simulation

of convective mixing in porous media coupled with carbonate geochemistry.

1.1. *Decoupled formulation for multispecies reactive transport*

The classic formulation of flow and transport in porous media coupled to geochemical

reactions is a set of mass balance equations for the relevant chemical species, namely the

ions and molecules participating in the chemical processes (Steefel & Lasaga 1994):

$$\phi\frac{\partial c_i}{\partial t} + \nabla \cdot (\mathbf{u}c_i) - \nabla \cdot (\phi D \nabla c_i) = r_i \qquad (i = 1, 2, \ldots, N_{\text{tot}}), \tag{1.1}$$

where c_i is the mass concentration of species i, r_i is the source/sink term of species i

due to chemical reactions (defined as the mass of species i produced/consumed in all

participating reactions per unit volume and unit time), N_{tot} is the number of aqueous

species, ϕ is porosity, $\mathbf{u}$ is the Darcy velocity and D is the diffusion/dispersion coefficient.

Equation (1.1) is then coupled with chemical reactions through appropriate relations for

the source/sink term.

When chemical reactions are slow compared to transport—a *reaction-controlled* system—

one can use a kinetic formulation for r_i to characterize the reactions. For example, a

simplified kinetic formulation to describe precipitation/dissolution of a mineral takes the

form (Steefel & Lasaga 1994):

$$r_i = \xi K f(c_m), \tag{1.2}$$

where ξ is the reactive mineral surface area, K is the kinetic rate constant associated

with dissolution/precipitation and $f(c_m)$ is some function of concentrations of the par-

ticipating species (c_m). Kinetic formulations similar to Eq. (1.2) have been adopted to

study dissolution patterns in fractured media (Detwiler & Rajaram 2007) and formation

of wormholes (Szymczak & Ladd 2011), both of which can exhibit slow chemical kinetics.

When reactions are fast, the problem becomes *transport-limited* because the reaction

time scale is much smaller than the transport time scale. In the limit of instantaneous

chemical equilibrium, the kinetic reaction rates become by definition infinitely large, but

the rates of production/consumption r_i remain bounded by the rate at which chemicals

are brought in contact to sustain the reactions.

A challenging aspect of reactive transport simulation is the high computational cost as

a result of the highly nonlinear nature of the coupled equations. To alleviate this compu-

tational burden, one can rewrite the mass balance equations through linear combinations

to eliminate the source/sink terms in all but a small subset of the transport equations

(Yeh & Tripathi 1991; Steefel & MacQuarrie 1996; Lichtner 1996; Saaltink *et al.* 1998).

Most reactive transport codes today employ variants of this split into primary and sec-

ondary chemical species (Yeh & Tripathi 1991; Olivella *et al.* 1996; Saaltink *et al.* 2004;

Xu *et al.* 2006; Hammond *et al.* 2012)

For the special case of geochemical systems described by instantaneous equilibrium

reactions, one can reformulate the problem as a transport equation for a *conservative*

species τ, defined as any quantity in the system that is unaffected by reactions.

$$\phi\frac{\partial \tau}{\partial t} + \nabla \cdot (\mathbf{u}\tau) - \nabla \cdot (\phi D \nabla \tau) = 0, \tag{1.3}$$

from which the rate of production/consumption r_i is determined by an analytical expres-

sion (De Simoni *et al.* 2005, 2007):

$$r_i = 2\phi F_i(\tau)\left(\nabla\tau \cdot D\nabla\tau\right). \tag{1.4}$$

Typical examples of the conservative variable τ include ionic charge (Andre & Rajaram

2005), or a given element such as carbon (De Simoni *et al.* 2005).

114   Equation (1.4) consists of two τ-dependent factors, both of which control where and

115   how much reaction occurs in a reactive transport system:

116   (a) The chemical speciation function of species i. Chemical speciation refers to the

117   distribution of a given element or ion amongst chemical species in the system. The

118   speciation function of element/ion i, defined here as $F_i(\tau) = \mathrm{d}^2 c_i / \mathrm{d}\tau^2$ (De Simoni et $al.$

119   2007), describes the vigor of the chemical reactions at a given system state (i.e, for a

120   given value of τ) and depends solely on the specifics of the reactions. It can be calculated

121    $\textit{offline}$, therefore greatly reducing the computational cost of the simulation.

122   (b) The scalar dissipation rate, $\varepsilon = \nabla\tau \cdot D\nabla\tau$, measures the local rate of fluid mixing

123   as a result of fluid flow and transport.

124   Loosely speaking, r_i is controlled locally by both the chemistry and the fluid mechanics.

125   This decoupled formulation (Eqs. (1.3)–(1.4)) has been shown to be a good approxima-

126   tion in systems with fast (but not instantaneous) reactions (Sanchez-Vila et $al.$ 2007). It

127   has been adopted by various authors to study reactions driven by fluid mixing, including

128   calcite dissolution in coastal carbonate aquifers (Rezaei et $al.$ 2005; Romanov & Drey-

129   brodt 2006; De Simoni et $al.$ 2007) and numerical modeling of laboratory experiments of

130   saltwater–freshwater mixing (Guadagnini et $al.$ 2009). In our system, the time to reach

131   geochemical equilibrium is estimated to be on the order of tens of hours, which is indeed

132   small compared to the time for flow and transport over the natural length scale in a typ-

133   ical aquifer (see appendix A). In situations where local transport time is comparable to

134   that of reaction, non-equilibrium effects can occur, although the finite-rate kinetics would

135   have minimal effect for the parameter ranges we investigate in this study (Sanchez-Vila

136   et $al.$ 2007). The above assumptions allow us to adopt the decoupled approach, which

137   also simplifies computation and offers insight into the interplay between geochemical and

138   hydrodynamic processes.

2. Mathematical formulation

We consider a two-dimensional porous medium with square geometry composed mainly of carbonate rocks, or $CaCO_3$ (figure 1). The porous domain has impermeable boundaries at the top and bottom, and we assume periodicity in the lateral direction. The height of the square domain is denoted H. There are two participating solutions in the system; *solution 1* consists of brine saturated with CO_2, and it enters the domain through the top boundary; *solution 2* is the ambient brine that initially fully saturates the porous medium. An important assumption we make in this formulation is that both solutions are initially at chemical equilibrium with the carbonate formation. This assumption is justified because 1) the pH for *solution 1* is around 4, which indicates fast reaction with the carbonate; 2) *solution 2* is the ambient brine, which has already reached chemical equilibrium with the carbonate during its geologic residence time. This assumption distinguishes our formulation from the classical kinetic reaction behavior. Under this setup, neither solution 1 nor solution 2 alone will induce reactions; rather it is the mixing of the two solutions, which disturbs local chemical equilibrium, that triggers geochemical reactions and rock dissolution. We assume Boussinesq, incompressible Darcy flow through porous media (Nield & Bejan 2006):

$$\nabla \cdot \mathbf{u} = 0, \quad \mathbf{u} = -\frac{k(\phi)}{\mu}(\nabla P - \rho g \mathbf{z}), \tag{2.1}$$

where $\mathbf{u}$ is the Darcy velocity, k is permeability, μ is dynamic viscosity, P is pressure, ρ is fluid density, g is gravitational acceleration and ϕ is porosity. We adopt a simple cubic law for the permeability–porosity relationship, $k = k_0(\phi/\phi_0)^3$, where k_0 and ϕ_0 are the initial permeability and porosity, respectively. This relationship captures the evolution in permeability induced by porosity increase observed in laboratory experiments (Carroll *et al.* 2013).
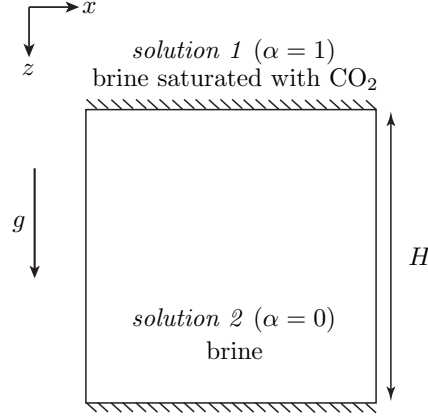
FIGURE 1. The problem is set up in a two-dimensional square homogeneous porous medium composed mainly of carbonate rocks. The domain is impermeable at the top and bottom. *Solution 1*, the equilibrated CO_2-rich brine, enters via diffusion at the top of the formation, which is initially saturated with *Solution 2*, the equilibrated aquifer-brine.

We denote the density of solution 1 as ρ_1 and that of solution 2 as ρ_2, where $\rho_1 > \rho_2$, and the density difference as $\Delta\rho = \rho_1 - \rho_2 > 0$. We define the mixing ratio α as the volumetric ratio of solution 1 in the mixture:
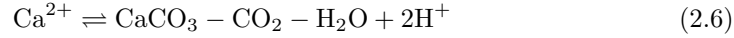
$$\alpha(x, z, t) = \frac{V_{\text{solution 1}}}{V_{\text{total}}}. \tag{2.2}$$

The density of the fluid mixture, ρ, increases linearly with the mixing ratio:

$$\rho = \rho_2 + \Delta\rho\, \alpha. \tag{2.3}$$

When the two solutions mix at α, chemical equilibrium is temporarily disturbed locally and the mixture undergoes a series of geochemical reactions to reach a new equilibrium with calcite. While this process can be complicated by the participation of other co-existing minerals such as magnesite ($MgCO_3$) or gypsum ($CaSO_4 \cdot H_2O$), the dominant effect can be captured with the following four reactions (Sanford & Konikow 1989; De

Simoni *et al.* 2007):

$$HCO_3^- \rightleftharpoons CO_2 + H_2O - H^+ \tag{2.4}$$

$$CO_3^{2-} \rightleftharpoons CO_2 + H_2O - 2H^+ \tag{2.5}$$

$$Ca^{2+} \rightleftharpoons CaCO_3 - CO_2 - H_2O + 2H^+ \tag{2.6}$$

$$OH^- \rightleftharpoons H_2O - H^+ \tag{2.7}$$

166   Eight chemical species participate in these reactions, namely calcium carbonate ($CaCO_3$),

167   water (H_2O), carbon dioxide (CO_2), hydrogen ion (H^+), bicarbonate (HCO_3^-), carbonate

168   (CO_3^{2-}), calcium ion (Ca^{2+}) and hydroxide (OH^-). Adopting the approach in De Simoni

169   *et al.* (2007) discussed in §1.1, we track the mixing ratio α, which is a conserved quantity

170   in the system equivalent to τ in Eq. (1.3), using the *advection–diffusion* equation:

$$\phi \frac{\partial \alpha}{\partial t} + \nabla \cdot (\mathbf{u}\alpha) - \nabla \cdot (\phi D \nabla \alpha) = 0, \tag{2.8}$$

171   where D is the diffusion/dispersion coefficient, taken here as constant. We assume here

172   that D is the same for all chemical species in the system and is also the same as that

173   of the fluid mixture. Using Eq. (1.4), we can then explicitly calculate the rate of calcite

174   dissolution, which according to Eq. (2.6) is also the production rate for Ca^{2+} :

$$r = 2\phi F(\alpha) \left(\nabla \alpha \cdot D \nabla \alpha \right), \quad F(\alpha) = \frac{\partial^2 [Ca^{2+}]}{\partial \alpha^2}, \tag{2.9}$$

175   where $F(\alpha)$ is the speciation term associated with Ca^{2+} that we obtain *a priori* with a

176   geochemical code such as PHREEQC (see appendix B). Equation (2.9) states that the

177   local rate of porosity change is controlled by two mechanisms: (1) chemical speciation of

178   calcium ion, $F(\alpha)$, which measures the vigor of the rock dissolution reaction in equation

179   (2.6), and (2) strength of fluid mixing, which is measured in terms of scalar dissipation

180   rate of α. Finally, we update porosity locally using the calcite dissolution rate r:

$$c_s \frac{\partial \phi}{\partial t} = r\Theta(\phi_1 - \phi), \tag{2.10}$$

181 where c_s is the molar density of calcite, and Θ is the Heaviside step function that limits

182 the increase in porosity to a maximum value ϕ_1, which accounts for the presence of

183 residual minerals that are nonreactive in the system. Once ϕ reaches ϕ_1 locally, the

184 assumption of chemical equilibrium fails since there is no more calcite to react with the

185 un-equilibriated mixtures; nevertheless, we assume equilibrium for solutions that pass

186 through the inert area . We keep this special case in mind and address its limitations

187 when we interpret the results in section 3.2.

188   We choose as characteristic velocity the speed at which a fluid parcel sinks in the porous

189 medium: $U_c = k_0 \Delta \rho g / \mu$. The natural length scale is the length over which diffusion and

190 advection are balanced: $L = \phi D / U_c$. We choose to rescale the problem with this intrinsic

191 length scale L as it is more relevant than domain height (H) for characterizing local

192 quantity changes. We set the other characteristic quantities as:

$$\rho_c = \Delta\rho, \;\; P_c = \Delta\rho g L, \;\; T_c = \frac{\phi_0 L}{U_c}, \;\; \phi_c = \phi_0, \;\; F_c = \max(|F(\alpha)|), \;\; r_c = \frac{2\phi_0 F_c D}{L^2}.$$

193 Applying these scales, we obtain three dimensionless parameters: the dimensionless do-

194 main height H $= H/L$, the maximum relative porosity increase $R_\phi = \phi_1/\phi_0$, and the

195 dissolution Damkhöler number:

$$\mathrm{Da} = \frac{r_c T_c}{c_s \phi_0} = \frac{2F_c}{c_s}. \tag{2.11}$$

Since we use the intrinsic length scale here, the Rayleigh number ($\mathrm{Ra} = U_c L / D$) is iden-

tically equal to one, and H plays the role of the traditional Ra (Hidalgo & Carrera 2009).

The dissolution Damkhöler number measures the competition between rock dissolution

rate and solute transport velocity. In dimensionless form, the governing equations read:

$$\nabla \cdot \mathbf{u} = 0, \quad \mathbf{u} = -\phi^3(\nabla P' - \alpha \mathbf{z}), \tag{2.12}$$

$$\phi \frac{\partial \alpha}{\partial t} + \nabla \cdot (\mathbf{u}\alpha) - \nabla \cdot (\phi \nabla \alpha) = 0, \tag{2.13}$$

$$\frac{\partial \phi}{\partial t} = \mathrm{Da}\, r \Theta(R_\phi - \phi/\phi_0), \quad r = \phi F(\alpha)(\nabla \alpha \cdot \nabla \alpha). \tag{2.14}$$

Here, P' is the dimensionless pressure with respect to a hydrostatic datum posed by ρ_2. The boundary and initial conditions are:

$$\alpha(x, z = 0) = 1, \quad \left.\frac{\partial \alpha}{\partial z}\right|_{x, z = \mathrm{H}} = 0,$$

$$\mathbf{u} \cdot \mathbf{n}(x, z = 0) = 0, \quad \mathbf{u} \cdot \mathbf{n}(x, z = \mathrm{H}) = 0,$$

$$\phi(t = 0) = 1, \quad \alpha(t = 0) = 0.$$

We adopt a stream function–vorticity formulation for Eq. (2.12) (Tan & Homsy 1988; Riaz & Meiburg 2003; Fu *et al.* 2013) and solve for the stream functions with an eighth-order finite difference scheme, implemented with a fast Poisson solver (Swarztrauber 1977). To evaluate the derivatives used in the transport equation (Eq. (2.13)) and consumption rate (Eq. (2.14)(b)), we use sixth-order compact finite differences in the vertical direction (Lele 1992) and a Fourier discretization along the horizontal direction, which we assume to be periodic. We integrate Eq. (2.13) and Eq. (2.14)(a) sequentially in time using a third-order Runge-Kutta scheme with dynamic time stepping (Ruith & Meiburg 2000). We accelerate the onset of the gravitational instability by perturbing the initial mixing ratios at the top boundary with small white noise (an uncorrelated Gaussian random function).
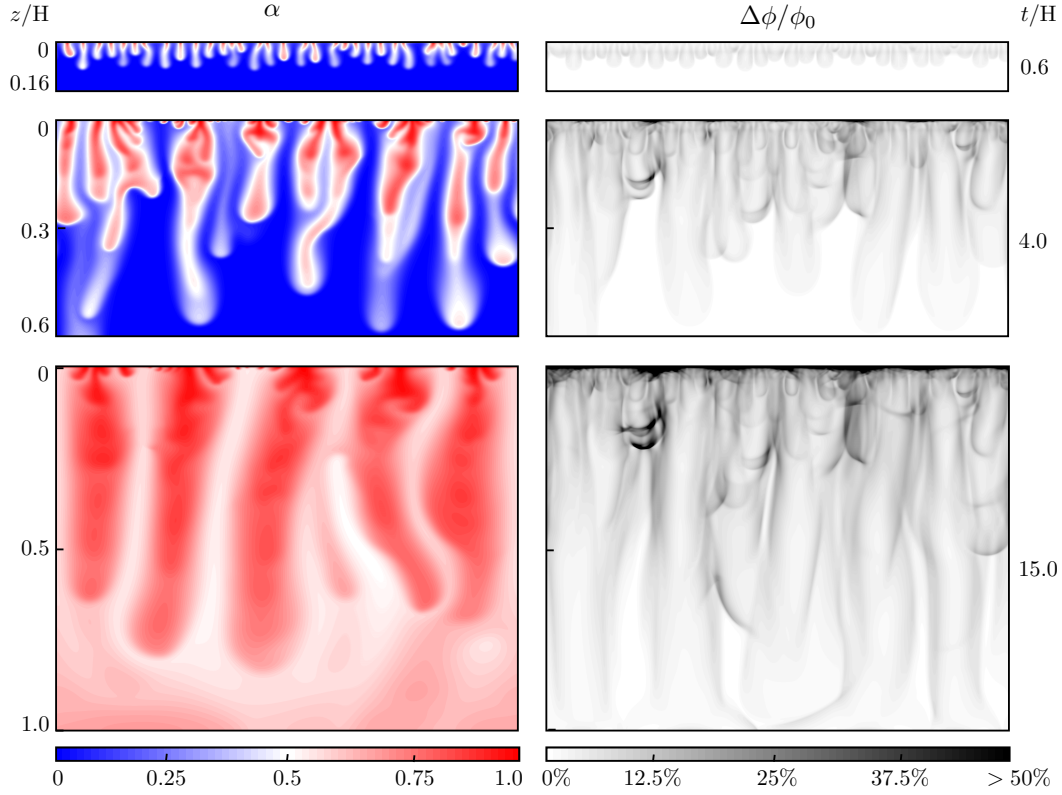
FIGURE 2. Snapshots of mixing ratio (left column) and porosity percentage increase (right column) for a simulation with H=6000, Da=20 and $R_\phi = 2$ at time $t = 0.6$H (top), 4H (middle) and 15H (bottom).

3. Dissolution regimes

In this section, we describe dissolution patterns as a result of the reaction with calcite, and we illustrate the various dissolution regimes. Specifically, we focus on $\langle \Delta\phi \rangle$, the domain-averaged porosity increase, and $\mathrm{d}\langle\alpha\rangle/\mathrm{d}t$, the time derivative of the domain-averaged pore-volume ratio of solution 1 (the equilibrated CO_2-rich brine), or cumulative mass of solution 1 in the domain. We solve the governing equations for Damkhöler numbers up to 20 and values of H up to 6000 on a grid of 2500^2 cells. Convergence tests show that the required grid resolution increases super-linearly with the product of H and Da since both parameters have a combined effect on generating small-scale details.

216   3.1. *Mixing-controlled dissolution patterns*

217   The diffusive layer of solution-1-rich mixture near the top boundary becomes gravita-

218   tionally unstable after some initial onset time, resulting in finger-like structures (figure

219   2, top left) that migrate downwards, stripping away the dense fluid (figure 2, middle left).

220   Fingering dynamics and scaling relations have been studied extensively (Riaz *et al.* 2006;

221   Hassanzadeh *et al.* 2007; Hidalgo & Carrera 2009; Hidalgo *et al.* 2012; Hewitt *et al.* 2013;

222   Slim *et al.* 2013; Slim 2014) and will not be the focus of this work. The density-driven flow

223   leads to mixing of fluids and triggers rock dissolution reactions which alter the perme-

224   ability field. Initially, these reactions chisel out patterns that follow closely the interface

225   of the fluid fingers, leaving the interior of these fingering channels almost unaffected

226   (figure 2, top and middle right). The "hollowness" of the dissolution patterns can be

227   understood as the direct consequence of a mixing-controlled dissolution rate (Eq. (1.4)).

228   The rate of fluid mixing, as measured by the scalar dissipation rate, is strongest along

229   finger interfaces where the concentration gradient is large (Hidalgo *et al.* 2012) and is

230   weak within the core of the fingers, where concentration gradients are small. Over time,

231   the rock dissolution patterns evolve in two ways:

232   (*a*) *Elongation towards the bottom:* new fingers are continuously born at the top bound-

233   ary; the cascade of fingers of different ages interact through a merging process where

234   young fingers merge into old ones, small ones into bigger ones, allowing the surviving

235   fingers to sink and coarsen laterally in size (Riaz *et al.* 2006; Hassanzadeh *et al.* 2007;

236   Pau *et al.* 2010; Slim 2014). As a result, finger-like dissolution channels continue to ex-

237   tend downwards and expand laterally (figure 2, bottom), following the locations of finger

238   interfaces where mixing is strong.

239   (*b*) *Focusing near the top:* while dissolution channels elongate towards the bottom due

240   to downward migration of fingers, regions of high rock dissolution, or "dissolution hubs"

241 start to appear near the top boundary (figure 2, bottom). These hubs develop as a result

242 of repeated events of newly born fingers carrying $\alpha \approx 1$ meeting the upwelling plume of

243 $\alpha \approx 0$, creating high concentration gradients that result in strong mixing and reaction.

3.2. Speciation-controlled reaction shutdown

245 The overall dissolution pattern is controlled by fluid mixing, as evidenced by the spa-

246 tial correlation between the permeability and mixing fields. However, the magnitude of

247 permeability increase, or how much reaction occurs when the two fluids mix, is set by

248 the shape of the speciation term $F(\alpha)$. As shown in figure 11 in appendix B, $F(\alpha)$ for

249 our geochemical system is a highly nonlinear function, showing that reaction is favored

250 in the lower range of mixing ratios ($\alpha < 0.1$); when $\alpha > 0.2$, $F(\alpha)$ becomes so small

251 that regardless of the strength of local mixing, almost no reaction will take place. The

252 behavior of this speciation curve is crucial for explaining the system's evolution.

253   For a simulation with H=6000, Da=20, we track the domain-averaged porosity increase

254 $\langle \Delta\phi \rangle$ with time, and find that after a period of monotonic growth, $\langle \Delta\phi \rangle$ reaches a plateau,

255 indicating a *shutdown* of dissolution reactions globally (figure 3(a)). We compute the

256 time for dissolution shutdown, $t_{\mathrm{sd}}^{\Delta\phi}$, as the time when $\langle \Delta\phi \rangle$ reaches 95% of the plateau

257 value, denoted $\langle \Delta\phi \rangle_{\mathrm{sd}}$; the shutdown times are shown as dark circles in figure 3(a). We

258 next track the domain-averaged speciation term over time and find that it also flattens

259 out towards zero after some period of time. We compute the corresponding time for

260 speciation shutdown, $t_{\mathrm{sd}}^{F(\alpha)}$, shown as dark circles in figure 3(b), as the time when $\langle F(\alpha) \rangle$

261 falls below 0.02. Shutdown time for dissolution corresponds closely to that of speciation

262 (figure 3(a) and (b), dark circles) and this shutdown happens much earlier than the

263 decaying of global degree of mixing (figure 3(c)). In other words, while reaction-inducing

264 fluid mixing is still active in the system, the fast decay of chemical speciation has caused

265 the dissolution reactions to stop at a much earlier time. We refer to this as a *speciation-*

₂₆₆ *controlled* reaction shutdown. The concept of convective shutdown was coined in the

₂₆₇ context of the one-sided convection system to describe the effect of domain saturation

₂₆₈ on the mass flux (Hewitt *et al.* 2013). Here, we find a shutdown in reaction caused by

₂₆₉ the decay of chemical speciation, not the loss in strength of the convective instability.

₂₇₀ We extend the above analysis to a range of values of H and Da, and find that the

₂₇₁ plateau value $\langle\Delta\phi\rangle_{sd}$ scales linearly with Da (figure 3(d)):

$$\langle\Delta\phi\rangle_{sd} \sim Da, \tag{3.1}$$

₂₇₂ which is a consequence of the role that Da plays in the porosity-update equation (Eq. (2.14)(a)).

₂₇₃ The shutdown time for dissolution and speciation both decrease with increasing Da (fig-

₂₇₄ ure 3 (e) and (f)). This is because as Da increases, the permeability near the top boundary

₂₇₅ increases faster, allowing fluid to enter and saturate the domain faster, and leading to an

₂₇₆ earlier speciation shutdown (see further discussion in §4). We find that H, on the other

₂₇₇ hand, has little impact on $\langle\Delta\phi\rangle_{sd}$ and $t_{sd}^{\Delta\phi}$, an observation that is consistent with the

₂₇₈ fact that the rate of fluid mixing is independent of H (Hidalgo *et al.* 2012).

₂₇₉ We analyze the time series of the porosity field and find that the maximum porosity

₂₈₀ ϕ_1 is reached locally for simulations with large Da and H after some initial period of

₂₈₁ dissolution and this critical time arrives later for smaller Da and H. This indicates that

₂₈₂ the special case of non-equilibrium state as discussed in section 2 is indeed present in

₂₈₃ some of our simulations. For small enough Da and H (e.g. H=2000 with any Da; H=4000

₂₈₄ with Da=1; H=6000 with Da=1), however, ϕ_1 is not reached anywhere. When ϕ_1 is

₂₈₅ reached, we find that the spatial spread of the non-equilibrium state is focused near the

₂₈₆ top boundary and accounts for a small portion of the domain, between 0.17% and 0.69%.

₂₈₇ This suggests that non-equilibrium effects are not critical in our examples. However, such

₂₈₈ non-equilibrium effect could be more important for simulations with large Damkhöler
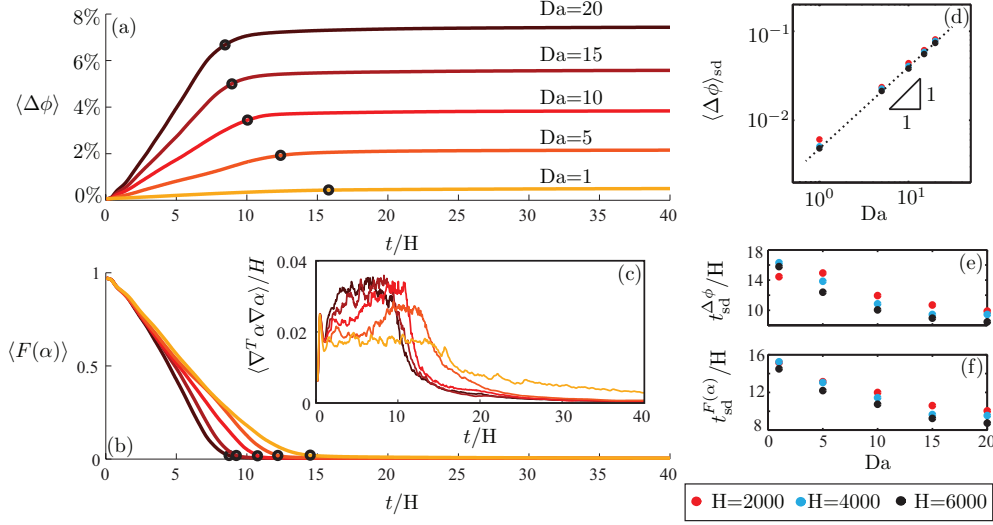
FIGURE 3. Volume-averaged measures of (a) percentage increase in ϕ (b) chemical speciation and (c) scalar dissipation rate over time for a simulation with H=6000. The transition in curve color from light orange to dark indicates increase in Da. The dark circles in (a) and (b) indicate the shutdown time $t_{sd}^{\Delta\phi}$ and $t_{sd}^{F(\alpha)}$, respectively, as defined in §3.2. (d) Cumulative (volume-averaged) porosity increase plotted against Da for different values of H (red, blue and black). (e) and (f) $t_{sd}^{\Delta\phi}$ and $t_{sd}^{F(\alpha)}$ plotted against Da for different values of H.

numbers as the maximum ϕ could be reached early on in the simulation and impact larger areas.

4. Impact on the macroscopic mass exchange rate

The macroscopic mass exchange rate measures how fast solution 1, the equilibrated CO_2-rich brine at the top, enters the formation and mixes with the resident brine. It is a quantity of special interest in the context of geologic carbon sequestration as it determines the effectiveness of solubility trapping. Previous studies that do not account for geochemical reactions (Hassanzadeh *et al.* 2007; Pau *et al.* 2010; Hidalgo *et al.* 2012; Hewitt *et al.* 2013; Slim *et al.* 2013; Slim 2014) have shown that the exchange rate, often referred to as the CO_2 flux, reaches a plateau after the onset of instability and

299 remains constant until domain saturation starts to impact the top boundary, at which

300 point the flux decays (figure 4, Da=0). Further, it has been shown that this constant flux

301 is independent of the domain size H (Hidalgo *et al.* 2012; Slim 2014). We address here

302 how these observations change in the presence of rock dissolution reactions.

303 We define the mass exchange rate as the volumetric flux of solution 1, $\mathrm{d}\langle\alpha\rangle/\mathrm{d}t$, which

304 we calculate by taking numerical derivative of $\langle\alpha\rangle$ with respect to t. For simulations

305 with fixed H (e.g. H=6000) and Da>1, we observe significant differences with respect

306 to the nonreactive case. Instead of reaching a plateau after the onset of convection,

307 the flux continues to grow with time as a result of increasing permeability from rock

308 dissolution near the top (figure 4, top); the rate of flux increase grows with Da. When Da

309 is sufficiently large (e.g. Da=20), the increase in $\mathrm{d}\langle\alpha\rangle/\mathrm{d}t$ hits a ceiling early on (figure 4,

310 top, Da=20); this is because the relative porosity increase $\langle\Delta\phi\rangle$ at the top has reached

311 R_ϕ and cannot increase further. In all cases, with or without reaction, the flux ultimately

312 decays due to the effect of domain saturation and, as shown in figure 4, the flux decays at

313 earlier times as Da increases. This is, again, because an increase in permeability leads to

314 a more convective system that can reach saturation faster. These observations are largely

315 independent of the values of H (figure 4, bottom), similar to what we observe in §3.2.

5. Dissolution patterns in three dimensions

317 We simulate equations (2.12)–(2.14) with the same boundary and initial conditions in

318 three dimensions, for a case with H=2500, Da=5 and R_ϕ=2 with a grid resolution of 368^3

319 cells. The numerical scheme is the same as that for 2D, where we use Fourier discretization

320 in the x and y directions and compact finite differences in the z-direction. Similar to the

321 2D results, the reaction shuts down at around t/H=8. We present the final morphology

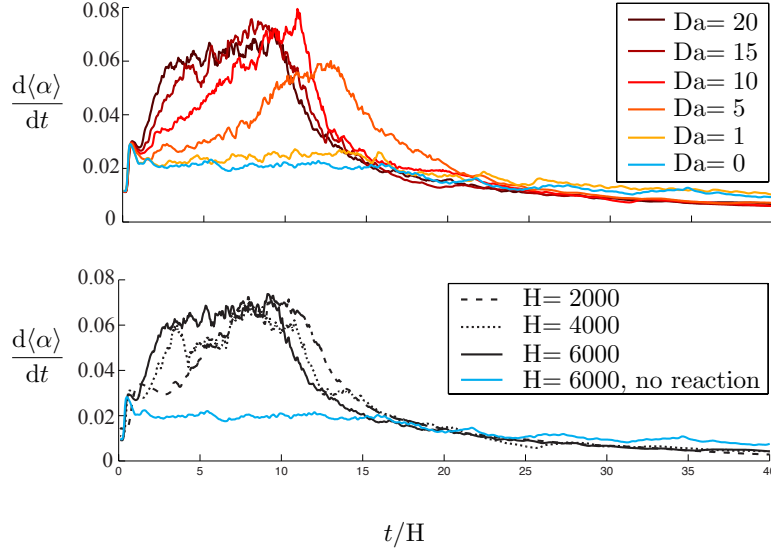322 (at t/H=14) of dissolved rock in figure 5. As the 3D columnar fingers move downwards—

FIGURE 4. Volume-averaged measure of mass exchange rate of solution 1 for increasing Damkhöler numbers with H=6000 (top) and for three values of H with Da=20 (bottom). The blue curves in both figures correspond to the case with H=6000 and without reaction (Da=0).

see more details in Fu *et al.* (2013))—they chisel out columnar-shaped regions along the

finger-brine interfaces (figure 5(a)) as a result of the high local concentration gradients.

Underneath the top boundary layer, the interiors of fingers are barely affected by reaction

(figure 7, (b)-(f), black-white frames). These empty columns are analogous to the hollow

channels observed in 2D (see §3.1). At the top boundary we observe the same dissolution

hubs as seen in 2D (§3.1); here, they take the shape of upside-down dunes, scattered and

hanging from the top surface (figure 5(b)).

While 3D visualization gives insight into the morphology of the rock dissolution pat-

terns, it provides limited quantitative details. To obtain more information about the

interior structure of the dissolution morphology, we plot horizontal slices of $\Delta\phi/\phi_0$ at

six depths: $z/\mathrm{H} = 0.01$ (top boundary layer), $z/\mathrm{H} = 0.14, 027, 0.54$ and 0.82 (the bulk)

and $z/\mathrm{H} = 1.0$ (bottom). As fingers start to arrive at a given depth, circular rings of dis-

solved rock emerge within the horizontal plane, reflecting the shape of fingering plumes at
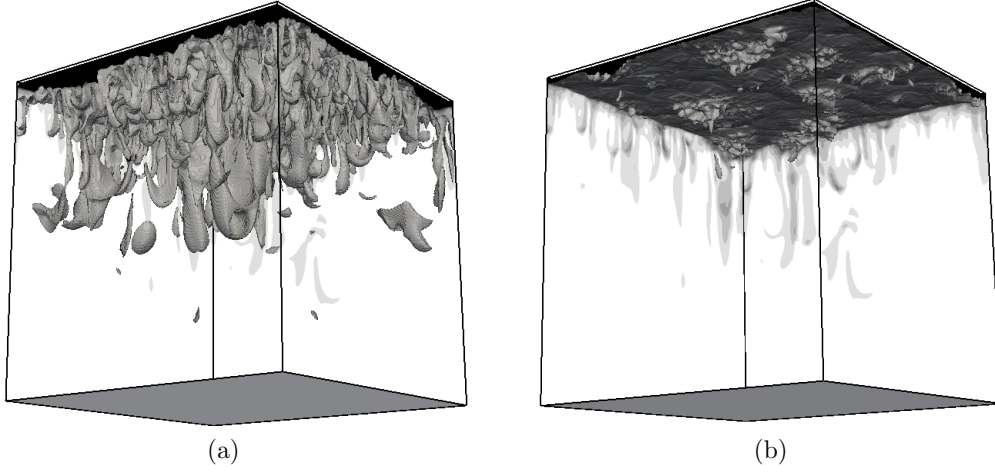
(a) (b)

FIGURE 5. Dissolution patterns in 3D: for a simulation of H=2500, Da=5 and R_ϕ=2, at $t/\mathrm{H} = 14.0$, this figure shows surface contours for (a) $\Delta\phi = 4\%$ and (b) $\Delta\phi = 8\%$.

336 those depths. With the exception of the top boundary layer ($z/\mathrm{H} = 0.01$), the dissolved

337 rings continue to expand laterally to form a tessellation of polygons. The polygons are

338 "hollow" inside and separated from each other by a clearly-defined polygonal network

339 of undissolved edges (figure 7(b)-(f), black and white frames). Once the tessellation has

340 evolved into its full form, usually within $\Delta t = 2500$ after the fingers invade that depth,

341 the pattern "freezes" in time due to a drastic reduction in dissolution activity.

342   We track the dissolution rate at each depth as a function of time—denoted here as

343 $\mathrm{d}\langle\phi\rangle_z/\mathrm{dt}$, where $\langle\cdot\rangle_z$ is the average across the x-y plane—and observe that the dissolution

344 rates peak at around the time that dissolution structures "freeze" at that depth (figure 6).

345 Similar to earlier observations in 2D (§3.2), the "freezing" of rock dissolution structures is

346 a consequence of a speciation-controlled reaction shutdown: once fingers arrive at a given

347 layer, dissolution reactions take place for a short period of time; once the layer becomes

348 weakly saturated with α (e.g. $\langle\alpha\rangle_z > 0.1$), the reactions stop. Figure 6 also clearly

349 demonstrates the temporal dynamics of the shutdown process: instead of occurring all at

350 once, the shutdown takes place at later times for deeper layers. Overall, this provides us
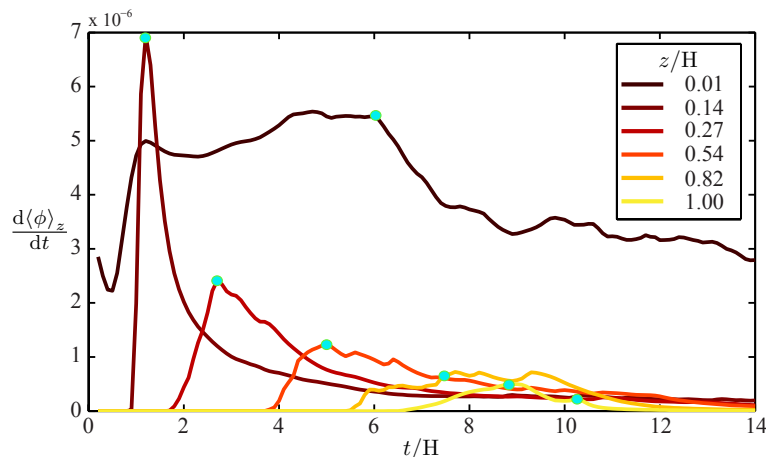
X. Fu et al.

FIGURE 6. Dissolution rate (laterally averaged) at various depths over time. Cyan-colored dots correspond to the "freezing" events, which is around the time that the tessellation pattern at that depth adopts its final configuration.

with a more mechanistic description on how these tessellation patterns evolve: as fingers arrive at each layer, they imprint their "images" through mineral dissolution onto the porosity field; once the reaction shuts down, the dissolution pattern becomes immune to further alterations by fingering dynamics.

5.1. *Coarsening of dissolution patterns*

Finger coarsening in nonreactive convective mixing has been observed and quantified in both experimental studies (Backhaus *et al.* 2011; MacMinn & Juanes 2013) and simulations (Fu *et al.* 2013; Hewitt *et al.* 2013; Slim *et al.* 2013). The dynamics of coarsening are different in the boundary layer and within the bulk. Near the top boundary, finger roots initially coarsen through a series of merging events but then reaches a statistical steady state, where the finger root spacing stands at a quasi-steady value (Fu *et al.* 2013; MacMinn & Juanes 2013). On the other hand, finger coarsening in the bulk persists throughout the entire lifetime of the falling fingers (MacMinn & Juanes 2013). In this work, because dissolution structures are directly linked to the spatial arrangement of
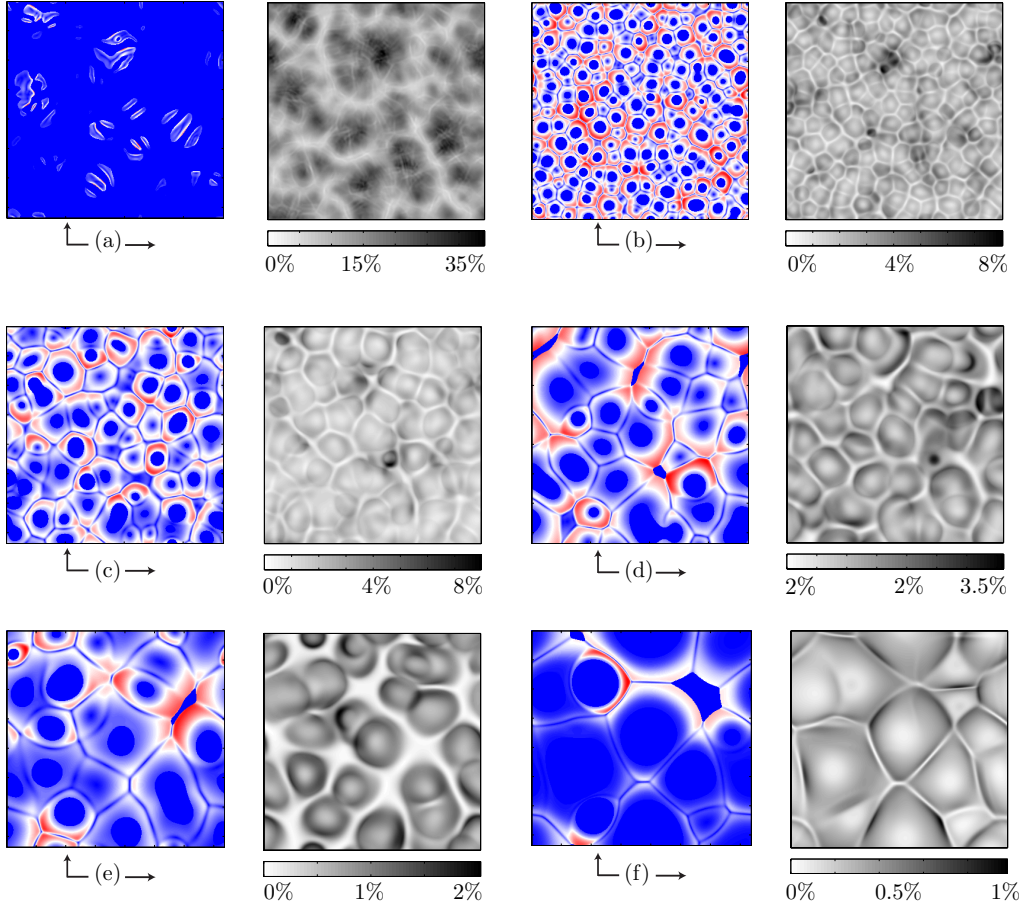
FIGURE 7. Horizontal slices of the reaction rate $r = \phi F(\alpha)\nabla\alpha \cdot \nabla\alpha$ (color frames) and the relative porosity increase $\Delta\phi/\phi_0$ (black and white frames) at different depths: (a) $z/H = 0.01$, (b) $z/H = 0.14$, (c) $z/H = 0.27$, (d) $z/H = 0.54$, (e) $z/H = 0.82$ and (f) $z/H = 1.0$. The color frames for r are at different times: (a) $t/H = 6.0$, (b) $t/H = 1.2$, (c) $t/H = 2.7$, (d) $t/H = 5.0$, (e) $t/H = 7.8$ and (f) $t/H = 10.1$ (subtracted from a background image corresponding to $t/H = 8.9$ for clarity). Red color indicates high value (colormap not shown). The black and white frames for $\Delta\phi/\phi_0$ are all at time $t/H = 14.0$. The colormap range varies with depth to best reflect the dissolution structure.

fingers, it is not surprising to find that the dissolution patterns also coarsen with depth (figure 7), much in the same way that fingers coarsen in the bulk. Here, we quantify this coarsening by counting the number dissolved polygonal rings (N_{polygon}) as a function of
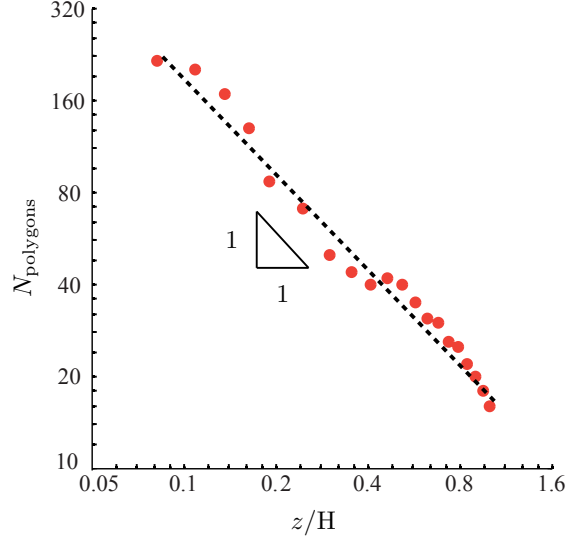
X. Fu et al.

FIGURE 8. Number of dissolved polygonal rings as a function of depth at $t = 14$.

depth (z), as seen in figure 7 (black and white frames) at $t = 14$ (figure 8). The analysis shows that the dissolution patterns coarsen with depth, and exhibit a robust power-law scaling:

$$N_{\text{polygon}} \sim z^{-1}. \tag{5.1}$$

The above scaling was suggested by an earlier study in 2D (MacMinn & Juanes 2013), where the number of fingers in the bulk is found to scale with convective time as: $N_{\text{fingers}} \sim t_{\text{conv}}^{-1}$. This is indeed consistent with Eq.(5.1) if we consider a constant finger falling speed so that $z \sim t_{\text{conv}}$. However, understanding the mechanism that leads to such scaling remains a future task in this study.

6. Summary

In this paper, we study rock dissolution as a result of geochemical reactions during convective mixing in porous media, in the context of CO_2 sequestration. To couple geochemistry with flow and transport, we assume a mixing-limited reactive transport system where reactions reach chemical equilibrium instantaneously compared to the transport

time scale. This allows us to adopt a formulation that completely decouples transport from reaction, and describes the local reaction rate as a function of scalar dissipation and chemical speciation (De Simoni *et al.* 2005). Using high-resolution simulations, we investigate the interplay between flow and reaction as a result of local permeability changes from rock dissolution. Because the reactive system we study here is mixing-limited, we find that the rate of rock dissolution is initially high in regions of high fluid mixing, which leads to dissolution patterns that closely follow the structure of the mixing field. However, geochemical reactions shut down much earlier than convective mixing shuts down; a result of the highly nonlinear behavior of chemical speciation. This feature of a *speciation-controlled* shutdown highlight the important role that the details of the geochemical equilibrium play in this hydrodynamics–reaction coupled process.

In both 2D and 3D simulations, we find that rock dissolution focuses on the top boundary, leaving the rock in the rest of the domain almost undissolved. As a result of the porosity increase at the top, we observe a significant increase in the rate at which the denser fluid enters the domain. This increase in solubility rate could enhance the effectiveness of CO_2 trapping in the context of a migrating plume (MacMinn *et al.* 2011). In the bulk, we see weak coupling from the rock dissolution patterns to the fingering dynamics, since the permeability increase is small below the boundary layer. We investigate the dissolution morphology in 3D and observe that the pattern at each depth exhibits a polygonal tessellation structure. This structure corresponds closely to the spatial arrangement of columnar fingers, and it also coarsens with depth in a similar way that convective fingers coarsen with time in the bulk of the domain.
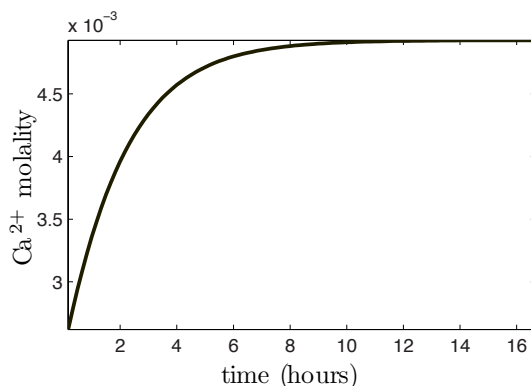
FIGURE 9. When solution 1 and 2 mix at $\alpha = 0.01$, concentration of Ca^{2+} in the mixed

solution increases over time as the mixture equilibrates over course of tens of hours.

7. Acknowledgement

Appendix A. Comparison between time to reach chemical

equilibrium and characteristic time of transport

The following analysis is specific to the chemical system in Eqs. (2.4)–(2.7) but can

be extended to other systems as well. We first estimate the time to reach chemical

equilibrium when solution 1 and 2 are mixed at a given α. We use the KINETICS data

block in PHREEQC (Parkhurst (1995)) and the Plummer-Wigley-Parkhurst rate model

for calcite dissolution (Plummer et $al.$ (1978)). Figure 9 plots calcium ion concentration

over time for a mixture of $\alpha = 0.01$, showing that equilibrium is reached at around $t = 10$

hours. We confirm with additional kinetic simulations that equilibrium is reached within

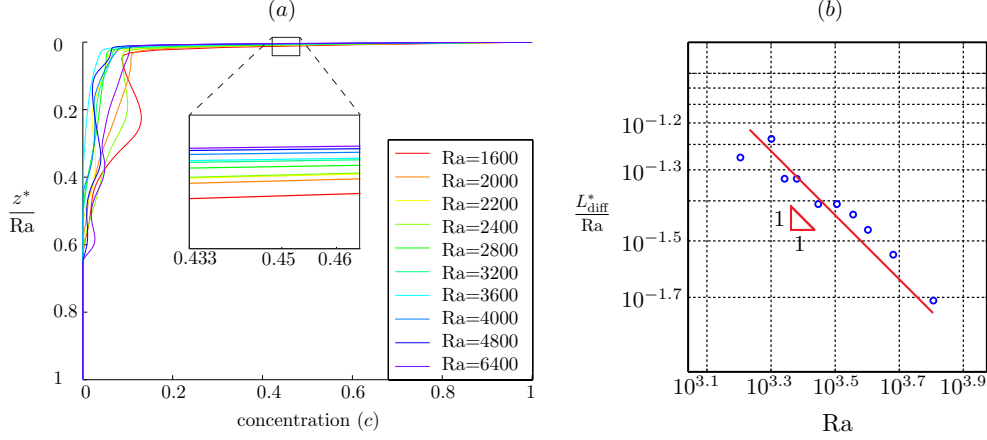tens of hours for all values of α (not shown here).

FIGURE 10. (a) Vertical concentration profiles at $t = 5$ for different Rayleigh numbers. We only show one sample of each Rayleigh number here while the analysis is done using ensemble of 5 samples for each Rayleigh number. Here $z^* = z/L$, where L is the natural length scale. (b) Average thickness of boundary layer, $L^*_{\mathrm{diff}} = L_{\mathrm{diff}}/L$, as a function of Rayleigh numbers.

418   We estimate the characteristic transport time across the natural length scale of the dif-

419   fusive boundary layer $L_{\mathrm{diff}} \approx 120\phi D/U$ to be on the order of thousands of hours or more

420   for a typical aquifer ($U = \Delta\rho g k/\mu$ is the characteristic velocity, where $k = 10^{-13}\mathrm{m}^2, D =$

421   $10^{-9}\mathrm{m}^2/\mathrm{s}, \Delta\rho = 10\mathrm{kg/m}^3, \mu = 0.8\times10^{-3}\mathrm{kg/m\cdot s}$). We obtain the coefficient of 120 in L_{diff}

422   by directly measuring the boundary layer thickness from 3D simulations. To quantify the

423   boundary layer thickness, we sample the vertical concentration profile, at $t = 5$, and at

424   five different horizontal locations; we repeat the sampling for different Rayleigh numbers

425   (figure 10a). We then define the boundary layer thickness as the depth below which the

426   concentration is smaller than $c = 0.3$. With this, we calculate the boundary layer thick-

427   ness for each sample and obtain the average thickness for each Rayleigh number (figure

428   10b). The fitted straight line in figure 10(b) suggests that

$$\log_{10}\left(\frac{L^*_{\mathrm{diff}}}{\mathrm{Ra}}\right) = -\log_{10}(\mathrm{Ra}) + 2.08,$$

429   which yields $L^*_{\mathrm{diff}} \approx 120$, or $L_{\mathrm{diff}} \approx 120\phi D/U$.
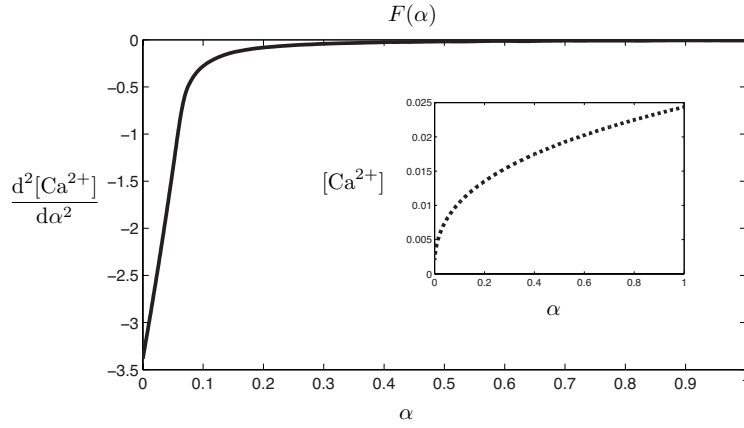
$$F(\alpha)$$

FIGURE 11. Speciation curve $F(\alpha)$ obtained from PHREEQC. The dashed line (inset) is the calcium molality ($[Ca^{2+}]$) versus α. The solid line (main plot) is the second derivative, computed numerically, of the dashed line.

Appendix B. Geochemical speciation curve

We use PHREEQC (Parkhurst 1995) to obtain the speciation curve corresponding to the chemical system in equations (2.4)–(2.7). To do so, we first define the composition of solution 1 and solution 2, which are the two fluids that participate in the mixing. To obtain solution 1, the equilibrated CO_2-rich brine, we subject pure water at pH $= 7$ and $T = 60°C$ to equilibrium with gaseous CO_2 at $pCO_2 = 10^2$ atm and with calcite. To obtain solution 2, the equilibrated aquifer-brine, we subject also pure water at pH $= 7$ and $T = 60°C$ to equilibrium with gaseous CO_2 at $pCO_2 = 10^{-1}$ atm and with calcite. Then, for one thousand, preselected and equally-spaced values of α, PHREEQC performs the speciation calculation by first mixing solutions 1 and 2 at volume fraction α and then re-equilibrating the mixed solution with respect to $CaCO_3$. At the end of each calculation, we obtain the value of calcium molality ($[Ca^{2+}]$) in the final mixed-and-equilibrated solution corresponding to that given mixing ratio (figure 11, inset). Finally, we calculate the speciation curve by taking the second derivative of the molality curve numerically (figure 11, solid curve).

445 The equilibrium constants of reactions in Eq. (2.4)–(2.7) are: $K_1 = 10^{6.3447}$, $K_2 =$

446 $10^{16.6735}$, $K_3 = 10^{-8.1934}$ and $K_4 = 10^{13.9951}$ respectively (Parkhurst 1995). These equi-

447 librium constants are corrected by the species activities γ_i, modeled using the extended

448 Debye–Hückel equation (Helgerson & Kirkham 1974):

$$\log\gamma_i = \frac{Az_i^2\sqrt{I_s}}{1 + \mathring{a}_i B\sqrt{I_s}} + \mathring{b}I_s, \tag{B 1}$$

449 where I_s is the ionic strength of the mixture characterized by α, z_i and $\mathring{a}_i$ are the valence

450 and the ionic radius of species i, respectively, and $\mathring{b}$, A and B are constants set by

451 PHREEQC.

REFERENCES

452 ANDRE, B. J. & RAJARAM, H. 2005 Dissolution of limestone fractures by cooling waters: Early

453   development of hypogene karst systems. *Water Resour. Res.* **41** (1), W01015.

454 BACKHAUS, S., TURITSYN, K. & ECKE, R. E. 2011 Convective instability and mass transport

455   of diffusion layers in a Hele-Shaw geometry. *Phys. Rev. Lett.* **106** (10), 104501.

456 BOLSTER, D. 2014 The fluid mechanics of dissolution trapping in geologic storage of CO_2. *J.*

457   *Fluid Mech.* **740**, 1–4.

458 CARROLL, S., HAO, Y., SMITH, M. & SHOLOKHOVA, Y. 2013 Development of scaling parameters

459   to describe CO_2-rock interactions within Weyburn-Midale carbonate flow units. *Int. J.*

460   *Greenh. Gas Control* **16**, S185–S193.

461 DE SIMONI, M., CARRERA, J., SÁNCHEZ-VILA, X. & GUADAGNINI, A. 2005 A procedure for

462   the solution of multicomponent reactive transport problems. *Water Resour. Res.* **41** (11),

463   W11410.

464 DE SIMONI, M., SÁNCHEZ-VILA, X., CARRERA, J. & SAALTINK, M. W. 2007 A mixing ratios-

465   based formulation for multicomponent reactive transport. *Water Resour. Res.* **43** (7),

466   W07419.

467 DETWILER, R. L. & RAJARAM, H. 2007 Predicting dissolution patterns in variable aperture

fractures: Evaluation of an enhanced depth-averaged computational model. *Water Resour. Res.* **43** (4), W04403.

ELKHOURY, J. E., AMELI, P. & DETWILER, R. L. 2013 Dissolution and deformation in fractured carbonates caused by flow of CO_2-rich brine under reservoir conditions. *Int. J. Greenh. Gas Control* **16**, S203–S215.

ENNIS-KING, J. & PATERSON, L. 2005 Role of convective mixing in the long-term storage of carbon dioxide in deep saline formations. *Soc. Pet. Eng. J.* **10** (3), 349–356.

FU, X., CUETO-FELGUEROSO, L. & JUANES, R. 2013 Pattern formation and coarsening dynamics in three-dimensional convective mixing in porous media. *Phil. Trans. R. Soc. A* **371**, 20120355.

GUADAGNINI, A., SANCHEZ-VILA, X., SAALTINK, M. W., BUSSINI, M. & BERKOWITZ, B. 2009 Application of a mixing-ratios based formulation to model mixing-driven dissolution experiments. *Adv. Water Resour.* **32** (5), 756–766.

HAMMOND, G. E., LICHTNER, P. C., LU, C. & MILLS, R.T. 2012 PFLOTRAN: Reactive flow and transport code for use on laptops to leadership-class supercomputers. In *Groundwater Reactive Transport Models* (ed. F. Zhang, G.T. Yeh & J. C. Parker), pp. 141–159. Sharjah, UAE: Bentham Science Publishers.

HASSANZADEH, H., POOLADI-DARVISH, M. & KEITH, D. W. 2007 Scaling behavior of convective mixing, with application to geological storage of CO_2. *AIChE J.* **53** (5), 1121–1131.

HELGERSON, H. C. & KIRKHAM, D. H. 1974 Theoretical prediction of the thermodynamic behaviour of aqueous electrolytes at high pressure and temperature: II Debye-Hückel parameters for activity coefficients and relative partial molol properties. *Am. J. Sci.* **274**, 11991261.

HEWITT, D. R., NEUFELD, J. A. & LISTER, J. R. 2013 Convective shutdown in a porous medium at high Rayleigh number. *J. Fluid Mech.* **719**, 551–586.

HIDALGO, J. J. & CARRERA, J. 2009 Effect of dispersion on the onset of convection during CO_2 sequestration. *J. Fluid Mech.* **640**, 441–452.

HIDALGO, J. J., FE, J., CUETO-FELGUEROSO, L. & JUANES, R. 2012 Scaling of convective mixing in porous media. *Phys. Rev. Lett.* **109**, 264503.

IPCC 2005 *Special Report on Carbon Dioxide Capture and Storage,* B. Metz et al. (eds.). Cambridge University Press.

KNEAFSEY, T. J. & PRUESS, K. 2010 Laboratory flow experiments for visualizing carbon dioxide-induced, density-driven brine convection. *Transp. Porous Media* **82**, 123–139.

LACKNER, K. S. 2003 A guide to CO_2 sequestration. *Science* **300** (5626), 1677–1678.

LELE, S. K. 1992 Compact finite difference schemes with spectral-like resolution. *J. Comput. Phys.* **103**, 16–42.

LICHTNER, P. C. 1996 Continuum formulation of multicomponent-multiphase reactive transport. In *Reactive Transport in Porous Media* (ed. P. C. Lichtner, C. I. Steefel & E. H. Oelkers), *Reviews in Mineralogy*, vol. 34, chap. 1, pp. 1–81. Washington, DC: Mineralogical Society of America.

LINDEBERG, E. & WESSEL-BERG, D. 1997 Vertical convection in an aquifer column under a gas cap of CO_2. *Energy Conv. Manag.* **38**, S229–S234.

MACMINN, C. W. & JUANES, R. 2013 Buoyant currents arrested by convective dissolution. *Geophys. Res. Lett.* **40**, 2017–2022.

MACMINN, C. W., NEUFELD, J. A., HESSE, M. A. & HUPPERT, H. E. 2012 Spreading and convective dissolution of carbon dioxide in vertically confined, horizontal aquifers. *Water Resour. Res.* **48**, W11516.

MACMINN, C. W., SZULCZEWSKI, M. L. & JUANES, R. 2011 CO_2 migration in saline aquifers. Part 2: Capillary and solubility trapping. *J. Fluid Mech.* **688**, 321–351.

NEUFELD, J. A., HESSE, M. A., RIAZ, A., HALLWORTH, M. A., TCHELEPI, H. A. & HUPPERT, H. E. 2010 Convective dissolution of carbon dioxide in saline aquifers. *Geophys. Res. Lett.* **37**, L22404.

NIELD, D. A. & BEJAN, A. 2006 *Convection in Porous Media*, 3rd edn. New York: Springer.

OLIVELLA, S., GENS, A., CARRERA, J. & ALONSO, E. E. 1996 Numerical formulation for a simulator (code_bright) for the coupled analysis of saline media. *Eng. Comput.* **13** (7), 87.

ORR, JR., F. M. 2009 Onshore geologic storage of CO_2. *Science* **325**, 1656–1658.

PARKHURST, D. L. 1995 *User's guide to PHREEQC: A computer program for speciation,*

reaction-path, advective-transport, and inverse geochemical calculations, water resources investigations report. Lakewood, Colo.

PAU, G. S. H., BELL, J. B., PRUESS, K., ALMGREN, A. S., LIJEWSKI, M. J. & ZHANG, K. 2010 High-resolution simulation and characterization of density-driven flow in CO_2 storage in saline aquifers. *Adv. Water Resour.* **33** (4), 443–455.

PLUMMER, L. N., WIGLEY, T. M. L. & PARKHURST, D. L. 1978 The kinetics of calcite dissolution in CO_2-water systems at $5°$ to $60°$C and 0.0 to 1.0 atm CO_2. *Am. J. Sci.* **278**, 179–216.

REZAEI, M., SANZ, E., RAEISI, E., AYORA, C., VÁZQUEZ-SUÑÉ, E. & CARRERA, J. 2005 Reactive transport modeling of calcite dissolution in the fresh-salt water mixing zone. *J. Hydrol.* **311**, 282–298.

RIAZ, A., HESSE, M., TCHELEPI, H. A. & ORR, JR., F. M. 2006 Onset of convection in a gravitationally unstable, diffusive boundary layer in porous media. *J. Fluid Mech.* **548**, 87–111.

RIAZ, A. & MEIBURG, E. 2003 Three-dimensional miscible displacement simulations in homogeneous porous media with gravity override. *J. Fluid Mech.* **494**, 95–117.

ROMANOV, D. & DREYBRODT, W. 2006 Evolution of porosity in the saltwater–freshwater mixing zone of coastal carbonate aquifers: An alternative modelling approach. *J. Hydrol.* **329**, 661–673.

RUITH, M. & MEIBURG, E. 2000 Miscible rectilinear displacements with gravity override. Part 1. Homogeneous porous medium. *J. Fluid Mech.* **420**, 225–257.

SAALTINK, M. W., AYORA, C. & CARRERA, J. 1998 A mathematical formulation for reactive transport that eliminates mineral concentrations. *Water Resour. Res.* **34** (7), 1649–1656.

SAALTINK, M. W., BATLLE, F., AYORA, C., CARRERA, J. & OLIVELLA, S. 2004 RETRASO, a code for modeling reactive transport in saturated and unsaturated porous media. *Geol. Acta* **2** (3), 235–251.

SAALTINK, M. W., VILARRASA, V., DE GASPARI, F., SILVA, O., CARRERA, J. & RÖTTING, T. S. 2013 A method for incorporating equilibrium chemical reactions into multiphase flow models for CO_2 storage. *Adv. Water Resour.* **62**, 431–441.

554 SANCHEZ-VILA, X., DENTZ, M. & DONADO, L. D. 2007 Transport-controlled reaction rates
555 under local non-equilibrium conditions. *Geophys. Res. Lett.* **34** (10), L10404.

556 SANFORD, W. E. & KONIKOW, L. F. 1989 Simulation of calcite dissolution and porosity changes
557 in saltwater mixing zones in coastal aquifers. *Water Resour. Res.* **25** (4), 655–667.

558 SLIM, A. 2014 Solutal-convection regimes in a two-dimensional porous medium. *J. Fluid Mech.*
559 **741**, 461–491.

560 SLIM, A., BANDI, M. M., MILLER, J. C. & MAHADEVAN, L. 2013 Dissolution-driven convection
561 in a Hele-Shaw cell. *Phys. Fluids* **25**, 024101.

562 STEEFEL, C. I. & LASAGA, A. C. 1994 A coupled model for transport of multiple chemical
563 species and kinetic precipitation/dissolution reactions with application to reactive flow in
564 single phase hydrothermal systems. *Am. J. Sci.* **294** (5), 529–592.

565 STEEFEL, C. I. & MACQUARRIE, K. T. B. 1996 Approaches to modeling of reactive transport
566 in porous media. In *Reactive Transport in Porous Media* (ed. P. C. Lichtner, C. I. Steefel
567 & E. H. Oelkers), *Reviews in Mineralogy*, vol. 34, chap. 2, pp. 83–129. Washington, DC:
568 Mineralogical Society of America.

569 SWARZTRAUBER, P. N. 1977 The methods of cyclic reduction, Fourier analysis, and the FACR
570 algorithm for the discrete solution of Poisson's equation on a rectangle. *SIAM Review* **19**,
571 490–501.

572 SZULCZEWSKI, M. L., HESSE, M. A. & JUANES, R. 2013 The evolution of miscible gravity
573 currents in horizontal porous layers. *J. Fluid Mech.* **736**, 287–315.

574 SZULCZEWSKI, M. L., MACMINN, C. W., HERZOG, H. J. & JUANES, R. 2012 Lifetime of
575 carbon capture and storage as a climate-change mitigation technology. *Proc. Natl. Acad.*
576 *Sci. U.S.A.* **109** (14), 5185–5189.

577 SZYMCZAK, P. & LADD, A. J.C. 2011 The initial stages of cave formation: Beyond the one-
578 dimensional paradigm. *Earth Planet. Sci. Lett.* **301** (3-4), 424–432.

579 TAN, C. T. & HOMSY, G. M. 1988 Simulation of nonlinear viscous fingering in miscible dis-
580 placement. *Phys. Fluids* **6**, 1330–1338.

581 WEIR, G. J., WHITE, S. P. & KISSLING, W. M. 1996 Reservoir storage and containment of
582 greenhouse gases. *Transp. Porous Media* **23** (1), 37–60.

XU, T., KHARAKA, Y. K., DOUGHTY, C., FREIFELD, B. M. & DALEY, T. M. 2010 Reactive transport modeling to study changes in water chemistry induced by CO_2 injection at the Frio-I Brine Pilot. *Chem. Geol.* **271** (3-4), 153–164.

XU, T., SONNENTHAL, E., SPYCHER, N. & PRUESS, K. 2006 TOUGHREACT—A simulation program for non-isothermal multiphase reactive geochemical transport in variably saturated geologic media: Applications to geothermal injectivity and CO_2 geological sequestration. *Comput. & Geosci.* **32** (2), 145–165.

XU, T. F., APPS, J. A. & PRUESS, K. 2003 Reactive geochemical transport simulation to study mineral trapping for CO_2 disposal in deep arenaceous formations. *J. Geophys. Res.* **108** (B2), 2071.

YEH, G. T. & TRIPATHI, V. S. 1991 A model for simulating transport of reactive multispecies components: Model development and demonstration. *Water Resour. Res.* **27** (12), 3075–3094.